Available online at www.sciencedirect.com
ScienceDirect
Trans. Nonferrous Met. Soc. China 30(2020) 727−745
Transactions of Nonferrous Metals Society of China
www.tnmsc.cn

An insight into microstructural heterogeneities formation between weld subregions of laser welded copper to stainless steel joints

Saranarayanan RAMACHANDRAN, A. K. LAKSHMINARAYANAN

Department of Mechanical Engineering, SSN College of Engineering, Kalavakkam 603103, Tamil Nadu, India

Received 9 May 2019; accepted 28 December 2019

Abstract: The effect of laser beam welding (LBW) process on the microstructure−mechanical property relationship of a dissimilar weld between the copper (Cu) and stainless steel (SS) was investigated. Backscattered electron (BSE) based scanning electron microscopy (SEM) imaging was used to characterize the highly heterogeneous microstructural features across the LBW (Cu−SS) weld. The BSE analysis thoroughly evidenced the complex microstructures produced at dissimilar weld interfaces and fusion zone along with the compositional information. Widely different grain growths from coarse columnar grains to equiaxed ultrafine grains were also evident along the Cu−weld interface. A high-resolution electron backscattered diffraction (EBSD) analysis confirmed the existence of the grain refinement mechanism at the Cu−weld interface. Both tensile and impact properties of the dissimilar weld were found to be closely aligned with the property of Cu base metal. Microhardness gradients were spatially evident in the non-homogeneous material composition zones such as fusion zone and the Cu−weld interface regions. The heterogeneous nucleation spots across the weld sub-regions were clearly identified and interlinked with their microhardness measurements for a holistic understanding of structure−property relationships of the local weld sub-regions. The findings were effectively correlated to achieve an insight into the local microstructural gradients across the weld.

Key words: laser beam welding; copper; stainless steel; microstructural characterization; tensile property; impact toughness

1 Introduction

In the field of modern and technologically progressive engineering materials, a significant focus has been made on identifying the feasibilities to join two distinct materials [1−5]. As a consequence of this, the requirements of the dissimilar material joint have been in an upward trend to aid the innovative challenges evolved in the current structural applications [6−11]. From the particular application perspective, all the existing materials have both merits/demerits in their physical/mechanical properties. Additionally, a single material is not capable of satisfying the needs of an application on a full scale. To fix this issue, any two competent materials that have entirely different physical/mechanical properties can be joined to serve the varying requirements involved in a critical application such as nuclear power generating structures. One such typical dissimilar material system considered for an exclusive investigation is copper (Cu) to stainless steel (SS) joint. The Cu−SS joint has been employed as a vital structural component in the nuclear reactor vessel [12,13], plasma fusion reactor [14], large vacuum chambers of particle accelerators at the National Synchrotron Light Laboratory (LNLS), Brazil [15] and the cryogenic mass flow meter [16]. Furthermore, the applications will be extended to other power generation and transmission components. This is due to the excellent electrical

Corresponding author: A. K. LAKSHMINARAYANAN; Tel: +91-44-27469700; Fax: +91-44-27469772;
E-mail: Lakshminarayananak@ssn.edu.in, akln2k2@yahoo.com
DOI: 10.1016/S1003-6326(20)65249-9

and thermal conductivities of Cu with the high corrosion resistance and superior mechanical properties of SS than Cu. Welding is a core joining technology and widely employed to join a wide range of dissimilar materials with sound mechanical properties. However, joining Cu with the SS through any fusion welding process will lead to some inevitable challenges due to the vast differences between their physical and mechanical properties. Despite the same crystal structure (FCC) of Cu and SS, the other contrasting properties especially their melting point and thermal conductivity will further compound the difficulties in the experimental approach of any fusion welding process. A few research studies have been attempted to avoid melting of the base materials (Cu and SS) using solid-state welding methods such as friction stir welding (FSW) [15,17−23] and explosive welding processes [24,25]. From a comprehensive review on these studies, it is inferred that the FSW process needs a costly tool material and optimum tool offset conditions. The explosive welding process involves a highly stringent safety regulations to manufacture a joint between Cu and SS. Fusion welding processes such as electron beam welding (EBW) [26,27] and gas tungsten arc welding (GTAW) [28−31] also have their limitations such as very high vacuum requirements and selection of an appropriate filler material, respectively. Laser beam welding (LBW) process has more advantages such as precise control of heat input, narrow heat-affected zone (HAZ), high energy density, no vacuum requirements, and being insensitive to the electromagnetic fields [32]. These characteristics along with other experimental flexibilities of LBW process have been responsible for its high impact in the field of welding dissimilar materials.

As Cu−SS joints have been serving in the critical nuclear industries, there is an absolute necessity to ensure the strength of the joint with a complete knowledge of microstructures across the weld. This is because the laser heat input combined with compositional gradients of the dissimilar materials can promote a local solidification process and grain growths. It is firmly believed that the backscattered electron (BSE) based SEM characterizations can spatially map the composition variations across the dissimilar weld. The majority of traditional SEM characterizations on dissimilar material systems have usually been performed through the secondary electron (SEI) signal instead of using the BSE signal. SEM/BSE characterization technique has been used on the dissimilar welded systems [33,34]. However, a clear difference received from the SEM/SEI, and SEM/BSE techniques on the same region of interest (ROI) has not been examined to date. Compared to SEM/SEI, the SEM/BSE technique can be preferred for characterizing any dissimilar material welded system wherever there will be considerable compositional gradients expected in the weld zone. This is because, the SEM/BSE characterization technique can be able to provide the compositional information through varying contrast in an image corresponding to the atomic number of the different elements located in the dissimilar weld. Moreover, a more detailed and high spatial resolution microstructural characterization technique such as EBSD is also needed to derive more quantitative information down to the resolution of grain size. The information obtained from the grain level can be used to compute the global strength of the weld by accounting the local microstructural changes. The LBW studies attempted to date on Cu−SS have contributed more to optimize the LBW process parameters to produce a sound LBW (Cu−SS) joint by effectively controlling the melting of Cu in the fusion zone [35−38]. It is clearly evident that the SEM/BSE and EBSD studies on the LBW (Cu−SS) weld have not been attempted elsewhere. In addition to this, the local microstructural changes across the LBW (Cu−SS) weld have not been correlated well along with other properties (tensile and microhardness measurements). Hence, this study has involved a range of material characterization techniques to reveal the local microstructure−mechanical property relationships of the LBW (Cu−SS) weld sub-regions. The findings achieved from the materials characterisation techniques are critically compared to add new knowledge on qualifying the dissimilar weld with a high degree of safety in the service environment.

2 Experimental

2.1 LBW process parameters optimization

The base metals used in this study were

C21000 copper alloy and 304 austenitic stainless steel sheets. For laser welding, all the as-received 2 mm-thick sheets were machined to dimensions of 300 mm × 150 mm, followed by milling to produce a uniform surface to weld. In advance to the welding process, the adjoining surface of the sheets was cleaned using 120 grit silicon abrasive paper followed by chemical cleaning using the acetone to degrease all thin oxide layers and other contaminations on the surface. A CO_2 laser welding system (Maker: TrumpF TruLaser Cell, Model: 7020) was used to manufacture the LBW (Cu−SS) joints for this investigation. From the critical literature review conducted on the studies related to LBW (Cu−SS) [33,36−38], it is inferred that the principal LBW process parameters needed to be optimized are laser power, welding speed, and laser beam offset conditions. Figure 1 shows the scatter between the literature findings on the optimized process parameters such as laser power versus welding speed. To select the optimum laser power and welding speed values from the scatter, this study had a series of experimental trials close to the optimized process parameters reported in the literature.

As plotted in Fig. 1, the optimum laser power and welding speed from the experimental trials are determined as (4±1.5) kW and (1.5±0.5) m/min, respectively. These values are found to be very close to the average value computed from the literature. To accomplish more clarity on the optimum laser beam offset conditions, this investigation had additional experimental trials by applying the above-mentioned optimized process parameters and also offsetting the laser beam towards the SS and Cu. It is noteworthy that the experiments executed by offsetting the laser beam towards the Cu have ended with a series of pores (as shown in Figs. 2(a−c)) due to the miscibility gap between the Cu and SS [39]. But the weld manufactured by offsetting the laser beam 0.2 mm towards the SS does not have any primary weld defects (as shown in Fig. 2(d)). This is because, the Cu is highly reflective to the laser beam, and therefore it has been advocated that the laser beam offset should be on the SS instead of Cu. The optimized process parameters, as reported in Table 1, were used to manufacture a defect-free LBW (Cu−SS) joint.

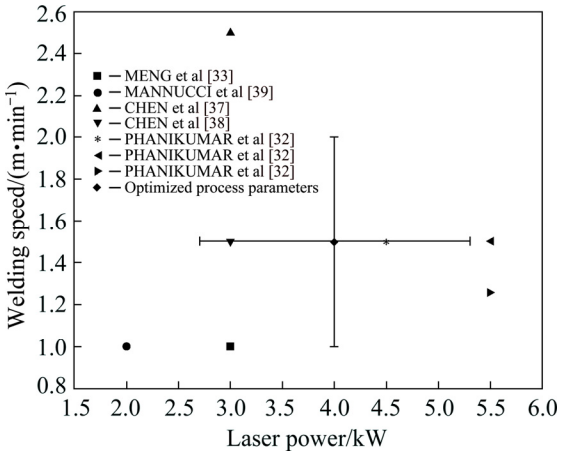

Fig. 1 LBW process parameters optimization

Table 1 Optimized LBW process parameters

Parameter	Description or value
Laser type	CO_2 laser, TRUMPF 7020
Laser power/kW	4
Welding speed/(m·min^{-1})	1.5
Feed/mm	20
Laser beam offset distance/mm	0.2 (Towards SS side)
Gas rate/(L·min^{-1})	15
Frequency/kHz	20
Inert gas	Argon

2.2 Materials characterization techniques

For the microstructural characterizations, the specimen was ground using silicon abrasive papers (1200, 4000 grit) followed by polishing through a diamond suspended chemical compounds (particle size: 6 μm, 1 μm). This polished stage was further extended using a fine Nap cloth suspended with a 0.04 μm colloidal silica solution for the EBSD analysis. The macrostructure of the specimen was observed using a stereomicroscope under very low magnification. To observe the microstructures across the weld cross-section, the mirror finish specimen was etched with the chemical mixture containing 25 g $FeCl_3$+25 mL HCL+100 mL H_2O for 10−15 s. It is noted that this chemical combination clearly revealed the microstructures both in the SS and Cu regions. The optical micrographs were captured using an optical microscopy (Maker: MEJI, Model MIL−7100) installed with an image analyzing software (Metal Vision).

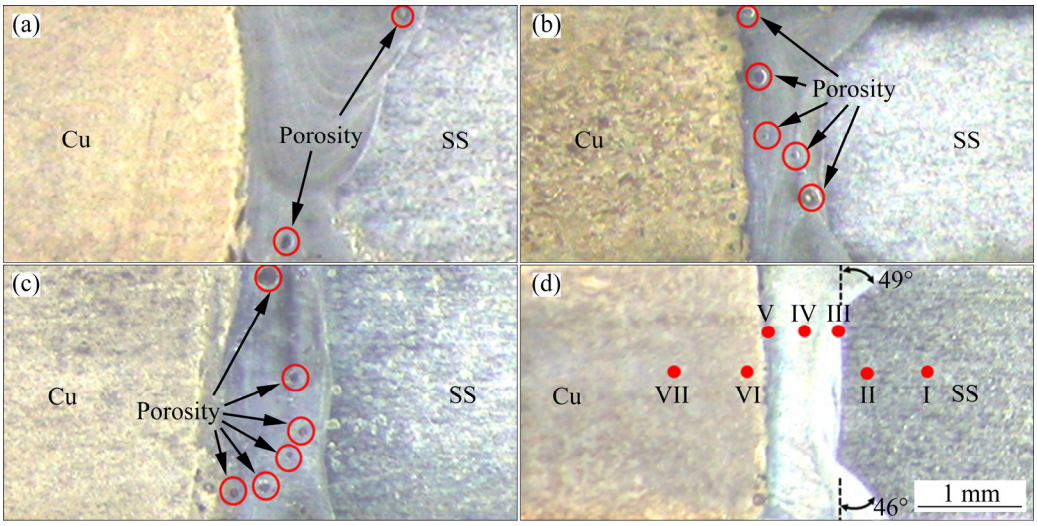

Fig. 2 Optical macrographs of LBW (Cu−SS) weld under different process parameters: (a) P=4 kW, V=1.5 m/min, ΔD (Cu)=0.2 mm; (b) P=4 kW, V=1.5 m/min, ΔD (Cu)=0.5 mm; (c) P= 4 kW, V=1.5 m/min, ΔD (Cu)=1 mm; (d) P= 4 kW, V=1.5 m/min, ΔD (SS)=0.2 mm (P−Laser power, V−Welding speed, ΔD−Laser beam offset distance)

For scanning electron microscopy (SEM) characterizations of the weld, the field-emission SEM (Maker: JEOL, Model: 7610F) was utilized at different magnifications in both the secondary and backscattered electron imaging modes (SEI and BSE) at an accelerating voltage of 15 kV. An energy dispersive X-ray spectroscopy (EDS) integrated with the SEM was used to map the chemical compositions in local regions across the weld. To perform a quantitative microstructural analysis, an EBSD (HKL Nordlys Detector with HKL channel 5 Flamenco software) characterization was executed at an accelerating voltage of 20 kV and probe current of 15 nA. Moreover, the EBSD analysis was performed using a low step size of 0.5 μm to measure the grain size and its misorientations in a high spatial resolution. The EBSD data files were post-processed by the Tango Map software for further analyses such as grain misorientation distributions, grain boundary populations, and grain size statistics.

All the transverse tensile specimens were machined in conformity to the ASTM E8M-16a sub-size standard [40] using an electric discharge machine (EDM). The standard tensile test was performed using the MTS servo-hydraulic test machine equipped with a 100 kN load cell at the displacement rate of 0.2 mm/min. For achieving consistency in the tensile results, three similar tensile specimens have tensioned to failure through a uniaxial tensile test. For impact toughness measurements, all the specimens were tested in conformity to the ASTM E23-12c standard [41] using a pendulum type Charpy impact testing machine. The microhardness measurements across the weld cross-section were made on the mirror finish specimen using a conventional microhardness tester (Maker: Mitsutoyo, Japan, Model: HV−112). To in line with the ASTM E384-17 standard [42], the spatial distance between the two successive hardness indents was 0.1 mm, and the indents were positioned at a load and dwell time of 50 g and 10 s, respectively.

3 Results

3.1 Optical macro/micrographs

Figure 2(d) shows the macro cross-section of the LBW (Cu−SS) weld with the local weld zones spatially positioned with respect to their grain morphology. The typical local weld zones along the Cu and SS sides are identified as follows: (I) SS-BM (base metal), (II) SS-HAZ, (III) SS−weld interface, (IV) fusion zone, (V) Cu−weld interface, (VI) Cu-HAZ, and (VII) Cu-BM. It is evident that a complete weld penetration through the thickness is achieved with the optimized LBW process parameters. The fusion zone does not have any major weld defects; this highlights the degree of confidence on the optimized process parameters adopted in this investigation. An average weld width measured from the top to bottom of the

fusion zone is (799±171) μm. This narrow dissimilar weld width without any extensive weld distortion can be produced only in the high power density and fast cooling rate based fusion welding process such as LBW [43]. The fusion zone has the slim-waist weld bead profile with a broad weld width in the top and bottom regions compared to the middle region. Furthermore, the fusion line close to the SS side is in the form of "W" shape with the top and bottom curved angles of 49° and 46°, respectively. However, the fusion line close to the Cu side is quite distinct with a slightly curved profile. Both the LBW process parameters and Marangoni convection effects have been responsible for the evolution of varying weld bead profiles in the dissimilar weld interfaces [44].

Figures 3(a−d) show the cross-sectional optical micrographs captured on the local weld zones. As expected, the SS-BM (Fig. 3(a)) shows the equiaxed austenite grains with annealing twins. There is no appreciable difference in grain size in the SS-HAZ region due to its structural stability at high temperature. The SS−weld interface exhibits the fine cellular dendritic microstructures. In contrast to the SS-interface zone, the fusion zone is partitioned with the equal volume of cellular dendrites and coarse columnar grains (Fig. 3(b)) due to the strong thermal gradients received from the laser heat. As the laser beam was completely offset towards the SS, apparently the Cu−weld interface should have a very minimum heat input compared to the SS. Additionally, a large scale of heat received from the fusion zone would be dissipated due to the high thermal conductivity of Cu. Thus, the fusion zone close to the Cu−weld interface with a small island of SS leads to the formation of the partially melted zone with a range of grain sizes, as exhibited in Fig. 3(c). The coarse columnar grains located in the Cu-weld interface have a grain growth normal to the boundary of the fusion line. The grain growth is noticed in the Cu-HAZ (Fig. 3(c)); Cu-BM has equiaxed Cu grains with scattered annealing twins, as shown in Fig. 3(d). It is noticeable that the LBW (Cu−SS) weld does not have any sharp interfaces either along the Cu or SS, which demonstrates that the dissimilar materials are well bonded with their weld interfaces despite laser beam was offset towards the SS.

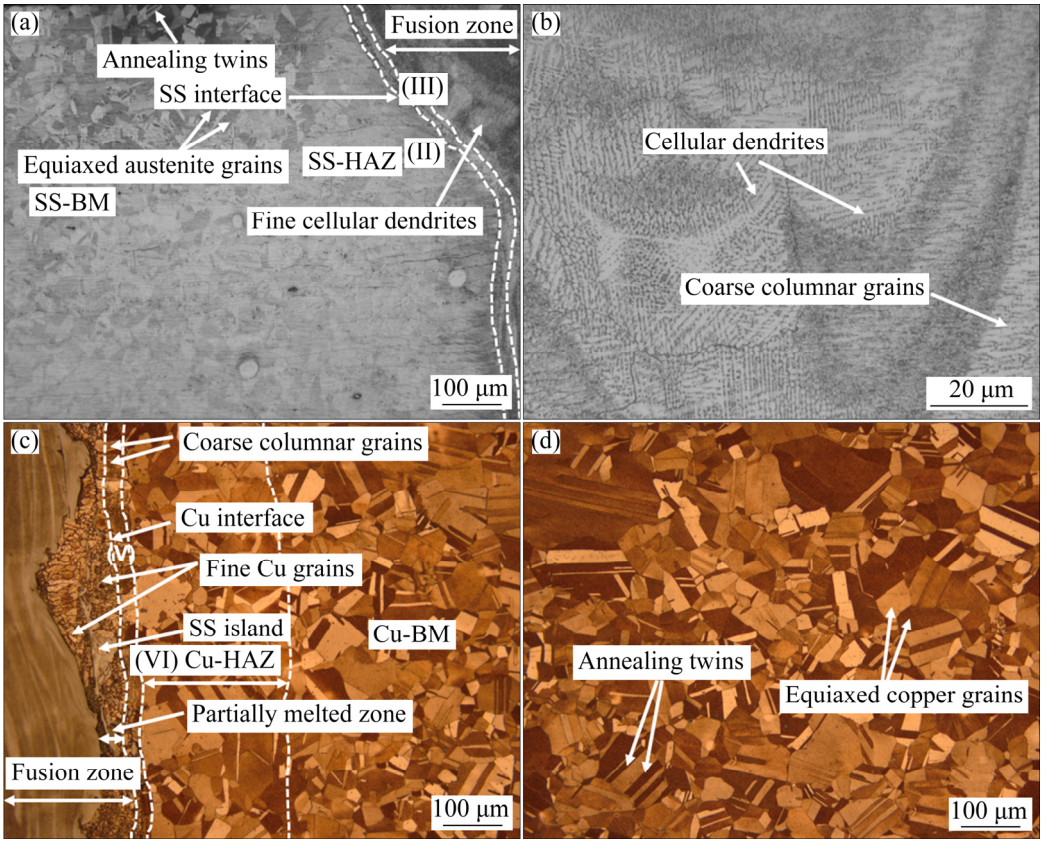

Fig. 3 Optical micrographs of local weld zones: (a) SS-BM and SS−weld interface (Zone I, Zone II and Zone III); (b) Fusion zone (Zone IV); (c) Cu−weld interface (Zone V and Zone VI); (d) Cu-BM (Zone VII)

3.2 SEM/SEI and SEM/BSE microstructural characterizations

It is a well-known theory that SEM/SEI and SEM/BSE characterization techniques can detect the secondary and backscattered electron signals respectively while imaging the specimen at very high magnifications inside the SEM vacuum chamber. The backscattered electrons (BSE) have higher energies than secondary electrons produced by the elastic collisions with atoms. By Heinrich's empirical relationship [45], the intensity of high energy backscattered electron coefficient of an element is directly related to its atomic number (Z):

$$\eta_{BSE}=0.025+0.016Z-1.86\times10^{-4}Z^2+8.3\times10^{-7}Z^3 \quad (1)$$

By applying the above polynomial relationship, the BSE coefficients of the base metals involved in this investigation, i.e., Fe (Z=26) and Cu (Z=29) phases, are determined as 0.28 and 0.30, respectively. Due to this minor difference between their BSE coefficients, a modest compositional contrast variation between the Fe and Cu elements can be observed through the SEM/BSE characterization on the fusion zone and dissimilar weld interfaces. For SEM/SEI and SEM/BSE characterizations, the regions S1, S2 and S3 along the stainless steel side interface and the regions C1, C2 and C3 along the copper side interface located in Fig. 4 were considered. The SEM/SEI and its corresponding SEM/BSE images captured at various locations are presented in Figs. 5 and 6. The primary objective of comparing the SEM/SEI and SEM/BSE results captured on the same ROI is to demonstrate the ability of the SEM/BSE technique to accomplish a clear insight into the microstructures and compositional variations simultaneously across a typical dissimilar weld.

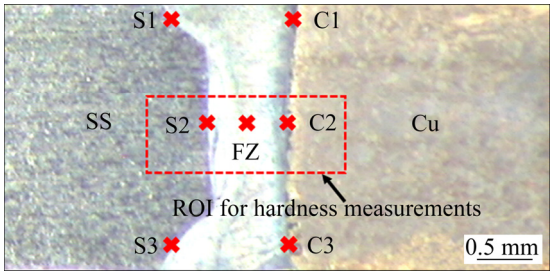

Fig. 4 Optical macrograph of LBW (Cu−SS) weld with ROIs for SEM/SEI and SEM/BSE characterizations (S1, S2, S3 are SS−weld interfaces, FZ means fusion zone and C1, C2, C3 are Cu−weld interfaces)

Figures 5(a−f) show SEM/SEI and SEM/BSE micrographs captured along the SS−weld interfaces. In contrast to the SEM/SEI (Figs. 5(a, c, e)), the SEM/BSE (Figs. 5(b, d, f)) micrographs captured along the SS-weld interfaces have an apparent contrast variation between the austenite and ferrite phases. As expected and mentioned elsewhere [46], the high chromium content (>18 wt.%) in the 304 SS has triggered the weld metal to primarily solidify as ferrite (BCC) and convert back to austenite (FCC) upon cooling at the end of weld solidification temperature. Austenite (γ) and ferrite (α) phases are represented by bright and dark features, respectively, in the SEM/BSE micrographs. As the laser beam was offset towards the SS, the fusion region close to the SS−weld interface has a typical austenitic microstructure with a range of dark ferrites. The formation of different ferrite phases was due to the high Cr_{eq}/Ni_{eq} ratio of 304 SS [46]. The fusion zone close to the S1 is completely packed with the cellular dendrites with a small portion of intercellular austenite (Fig. 5(b)). It is evident that the microstructure close to the interface S2 is entirely distinct from the S1 where the δ-ferrite has converted to lathy (lacy) and skeletal (vermicular) ferrites. The formation of these ferrites was due to varying chromium content activated during the weld solidification where the chromium rich region has transformed into dark ferrite on the austenite matrix. In addition to that, some branches of skeletal ferrites penetrated into the SS−weld interface (S2), as displayed in Fig. 5(d). An epitaxial grain growth with a dense population of δ-ferrites is observed in the fusion zone close to the SS−weld interface (S3) (as shown in Fig. 5(f)).

It has been mentioned elsewhere [46,47] that, the quantity of δ-ferrite generated in the fusion zone is directly proportional to the cooling rate of the welding process. The diverse microstructural morphologies of the SS-interfaces may be due to the turbulence in the weld solidification modes caused by the high cooling rate of LBW process. Thus, the steep thermal gradients involved in the LBW process have modified the Cr_{eq}/Ni_{eq} ratios in the SS-interfaces (S1, S2 and S3), which resulted in varying microstructural features in these interfaces. Moreover, all the weld interfaces of SS are very smooth instead of sharp which again confirmed the complete weld penetration. In the previous

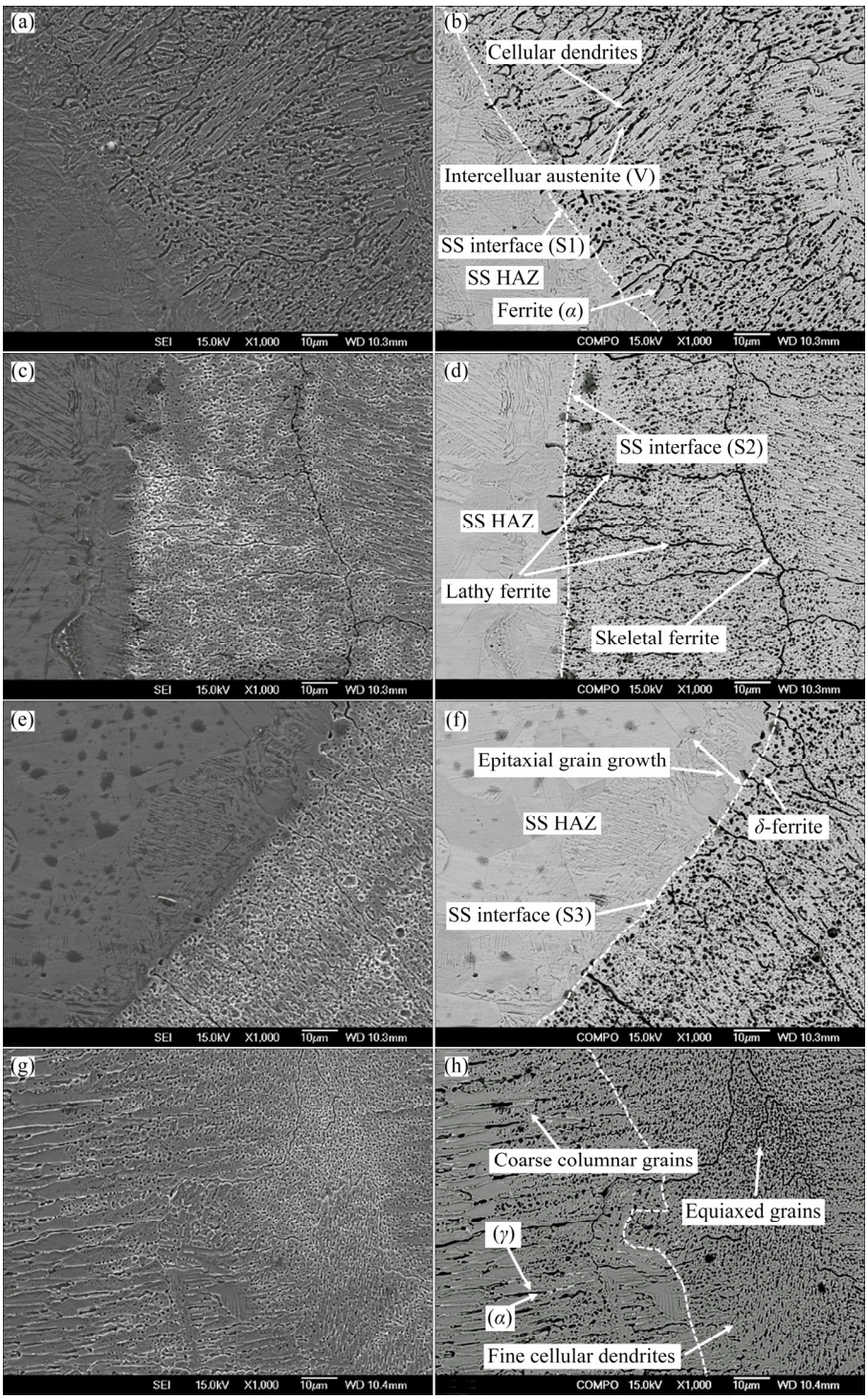

Fig. 5 SEM/SEI and its corresponding SEM/BSE micrographs of SS−weld interfaces and fusion zone: (a) S1, SEI; (b) S1, BSE; (c) S2, SEI; (d) S2, BSE; (e) S3, SEI; (f) S3, BSE; (g) Fusion zone, SEI; (h) Fusion zone, BSE

studies [36,38], the penetration of copper into the fusion zone has been qualitatively determined. But in this investigation, the range of findings offered by the SEM/BSE micrographs (Fig. 5) confirmed that the fusion zone has only austenite and ferrite phases without any major traces of Cu. Figures 5(g, h) show the SEM/SEI and SEM/BSE micrographs of the fusion zone, respectively. From this SEM/BSE image, it is observed that the fusion zone has a mixture of coarse columnar grains and fine equiaxed cellular dendrites.

The growth of all columnar grains is perpendicular to the weld pool with a minor scale of intercellular austenite (γ). The formation of coarse columnar grains in the fusion zone confirms the influence of high thermal conductivity of Cu

elements in this zone that resulted in abnormal grain growth. However, the Cu distribution in the fusion zone is not explicitly revealed from the SEM/BSE image. This is because the laser beam was offset towards the SS, and therefore apparently the weld fusion zone should have a more considerable quantity of Fe than Cu. Thus, a significant contrast variation between Fe and Cu elements does not appear in the SEM/BSE image.

Figures 6(a−f) show the SEM/SEI and SEM/BSE micrographs captured along the Cu−weld interfaces. The SEM/BSE image of the C1 interface (Fig. 6(b)) has exposed the presence of Cu elements along with SS in the fusion zone close to this interface. A high-intensity laser source combined with molten liquid of SS has controlled the effects of high thermal conductivity of Cu which melted the Cu in C1 and mixed it into the fusion zone. However, the high intensity of the laser beam did not penetrate further down from the C1 interface, which led to the creation of partially melted zone with a columnar grain growth along the fusion line close to the C2 (as shown in Fig. 6(d)). The reason behind this microstructural evolution is the supercooling effects offered by the combined high cooling rate of laser and high dissipation capability of Cu. As a consequence of these effects, a wide miscibility gap between SS and Cu elements is detected in the form of scattered SS islands on the Cu matrix close to the C2 interface, as shown in the SEM/BSE image of C2. Furthermore, the sharp compositional fluctuations triggered by the non-uniform melting of Cu into the fusion zone are responsible for different

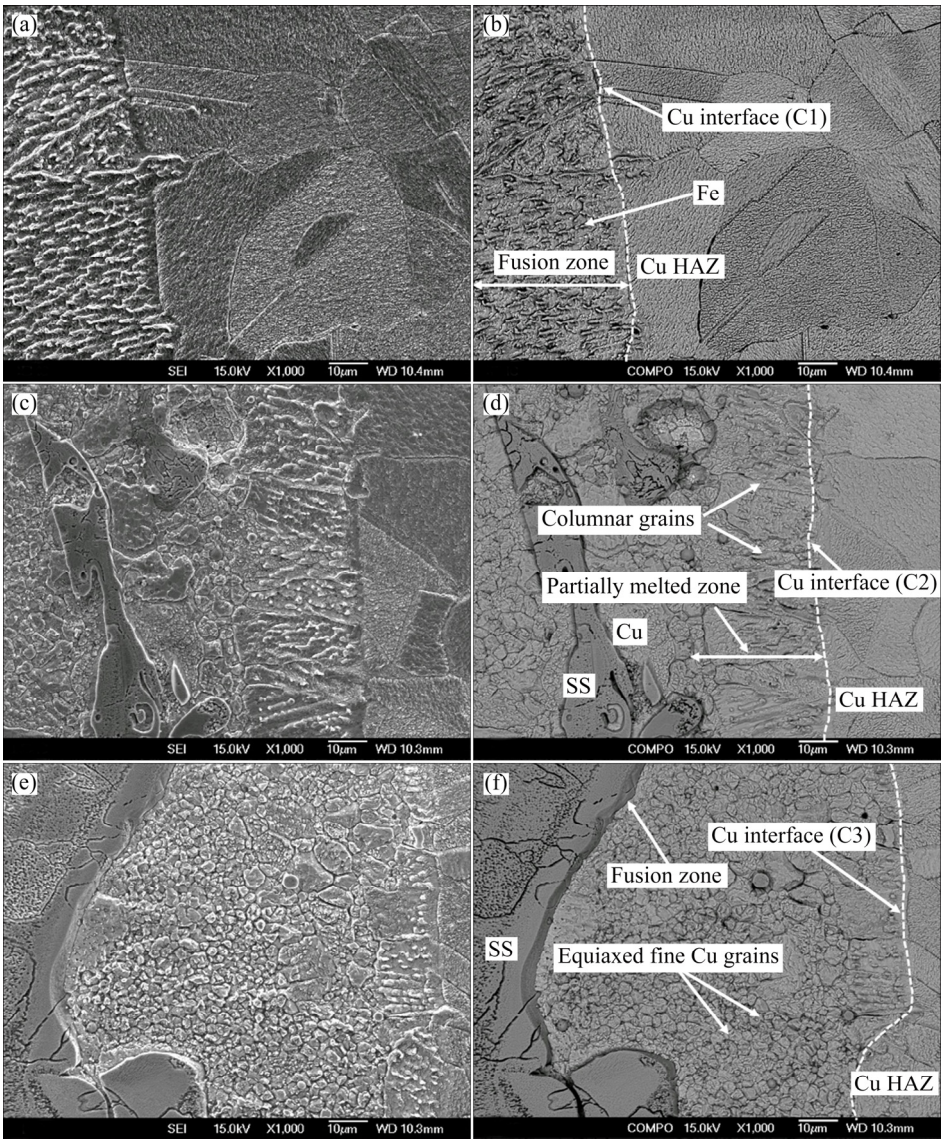

Fig. 6 SEM/SEI and its corresponding SEM/BSE micrographs of Cu−weld interfaces: (a) C1, SEI; (b) C1, BSE; (c) C2, SEI; (d) C2, BSE; (e) C3, SEI; (f) C3, BSE

microstructural features exhibiting close to the C2 interface. Due to even less heat input compared to C1 and C2, more quantity of fine equiaxed Cu grains without any microsegregation of Fe and Cu elements are observed in the region close to the C3 interface (as shown in Fig. 6(f)). Moreover, the heterogeneous nucleation mechanism promoted by the partially melted zone (C3) frozen with the liquid SS is responsible for the grain refinements in the region close to C3 [46]. All the valuable findings received through the SEM/BSE micrographs have unambiguously identified the spatial distribution of Cu and SS elements across the weld interfaces and fusion zone.

3.3 SEM/BSE−EDS analysis

In this study, the EDS chemical composition analyses were performed on the SEM/BSE image instead of SEM/SEI to achieve more consistency with the findings derived from the SEM/BSE characterizations discussed in the previous section. In addition, the SEM−EDS elemental mapping analyses of this study have only considered the main elements such as Fe and Cu by ignoring all other minor alloying elements of the base metals. The SEM−EDS elemental maps of Fe and Cu distributing on the SS−weld interfaces, fusion zone, and the Cu−weld interfaces are shown in Figs. 7(a−c), Fig. 7(d) and Fig. 8, respectively.

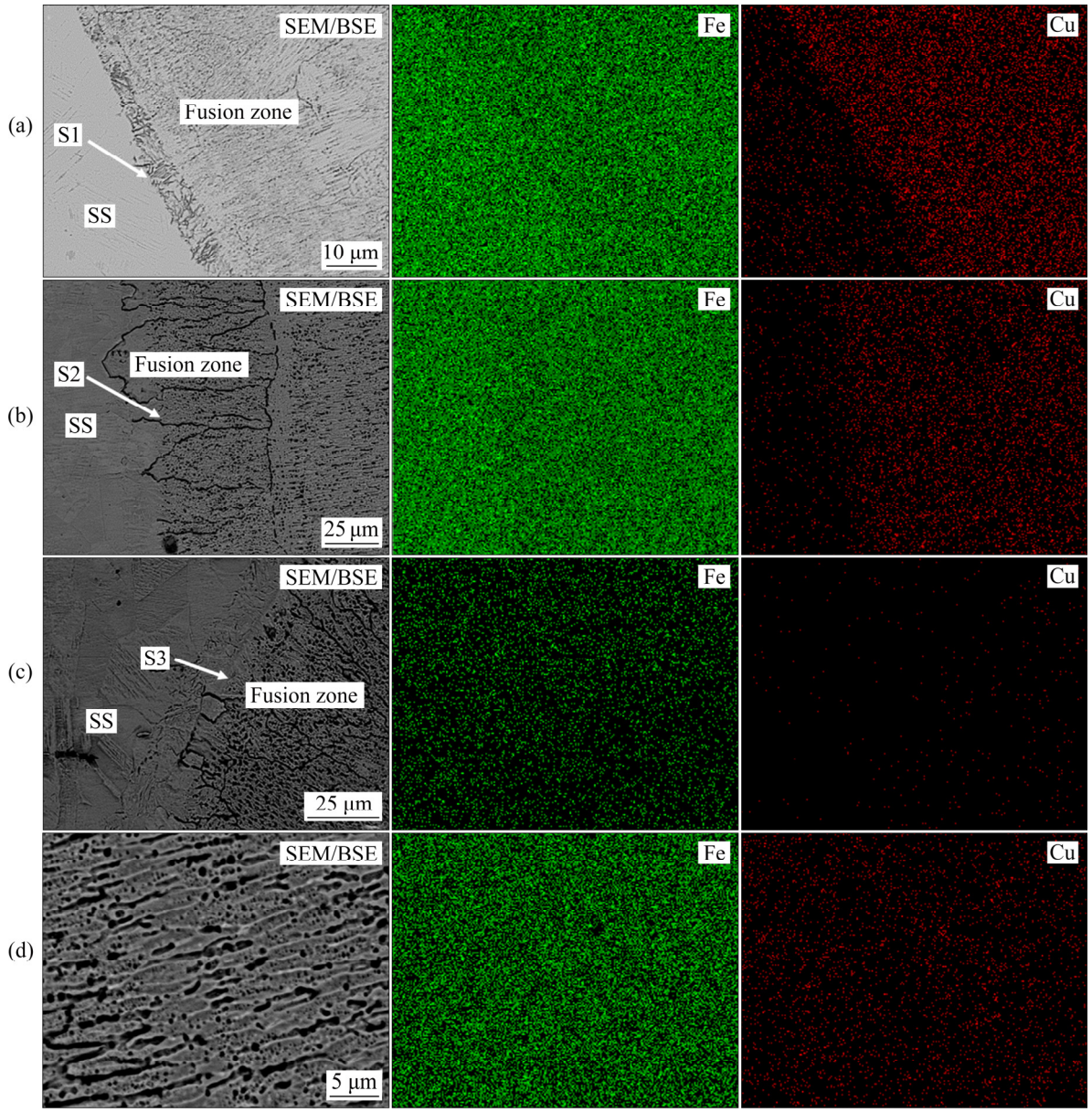

Fig. 7 SEM−EDS maps of Fe and Cu elements along SS−weld interfaces and fusion zone: (a) S1; (b) S2; (c) S3; (d) Fusion zone

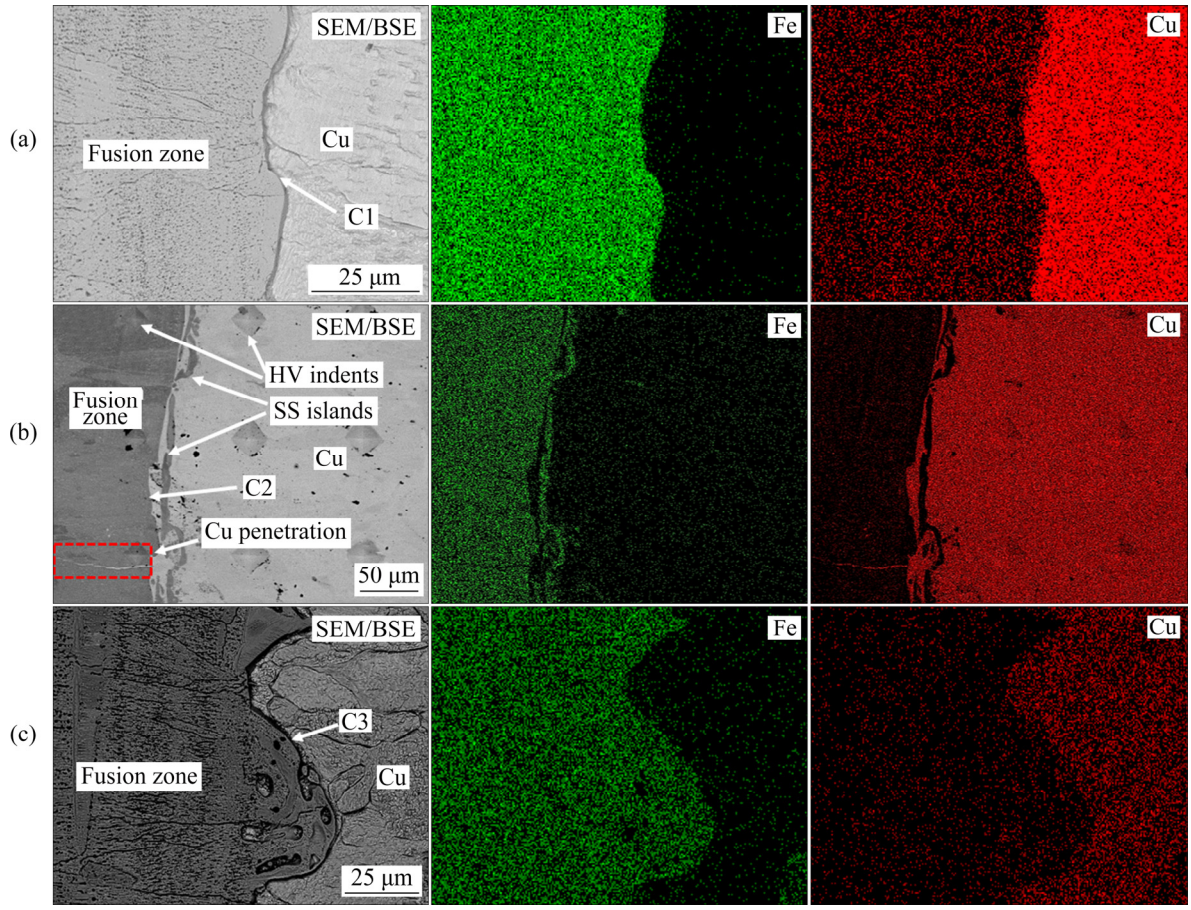

Fig. 8 SEM−EDS maps of Fe and Cu elements along Cu−weld interfaces: (a) C1; (b) C2; (c) C3

The EDS counts (in at.%) of main alloying elements computed from the corresponding EDS maps are listed in Table 2. Figures 7(a−d) show that the fusion zone has enriched with Fe, and there is no evidence for the large scale Cu migration routes into the SS−weld interfaces. Despite low mutual solubility between Cu and Fe, some minor Cu traces along with Fe are observed in the fusion zone. This confirmed that the metallurgical reaction between the Fe and Cu elements is inevitable [36]. However, the amount of Cu distributing in the fusion zone is almost negligible compared to Fe distribution as listed in Table 2, and thus the laser beam offsets towards the SS had a severe impact in controlling the Cu populations entering into the fusion zone. Additionally, there are no visible sharp SS−weld interfaces (S1, S2 and S3), which again proved the complete weld penetration in a high degree of confidence. It is noteworthy that the amounts of Fe counts along the SS−weld interfaces (67.73 at.% at S1, 68.09 at.% at S2 and 69.43 at.% at S3) and fusion zone (66.17 at.%) are almost homogeneous.

Table 2 EDS elemental compositions of weld interfaces and fusion zone (at.%)

Region	Cr	Mn	Fe	Ni	Cu	Zn
SS-BM	18.14	0.95	72.78	8.13	–	–
Cu-BM	–	–	–	93.68	6.32	–
S1	17.42	1.40	67.73	6.32	7.13	–
S2	17.54	1.31	68.09	6.52	6.54	–
S3	17.20	1.91	69.43	7.25	4.21	–
FZ	16.30	1.49	66.17	5.93	9.84	0.27
C1	9.43	0.71	31.26	3.23	52.91	2.46
C2	8.14	0.70	34.75	2.50	50.58	3.33
C3	10.36	0.70	34.16	3.48	49.48	1.82

The SEM−EDS analyses of the Cu interfaces (C1, C2, C3) shown in Fig. 8 have offered a large scale of critical observations. Firstly, all the maps show the distinct Cu−weld interface without any primary weld defects. In the C1 (Fig. 8(a)), both Cu and Fe elements diffuse in the fusion zone (Fe 31.26 at.%, Cu 52.91 at.%) better than C2 (Fe 34.75 at.%, Cu 50.58 at.%) and C3 (Fe 34.16 at.%, Cu 49.48 at.%). These compositional fluctuations

are interlinked with the turbulence of laser heat input caused by the high thermal conductivity of Cu. Secondly, the dark SS islands noticed on the bright Cu matrix (SEM/BSE micrograph) close to C2 are mapped as Fe in its corresponding EDS map. This makes an excellent correlation between the SEM/BSE and EDS findings on the compositional variations.

As spotted in the SEM/BSE image of Fig. 8(b), the Cu penetration into the fusion zone through a small channel is evidenced. The above observations made on the C2 have postulated the existence of the partially melted zone close to the C2 interface. In contrast to C2, there is no extensive occupancy of scattered Fe particles in the region close to C3 and also no evidence of specific Cu migration routes between the C3 interface and fusion zone (Fig. 8(c)). The key results derived from the SEM/BSE and its corresponding EDS maps completely corroborate the SEM/BSE results discussed in the previous section.

3.4 SEM−EBSD microstructural analysis

3.4.1 Grain orientations

Figure 9 shows the high spatial resolution inverse pole figure (IPF) maps of the local weld sub-regions. The IPF maps represent the directions of the grain orientations such as ⟨100⟩, ⟨110⟩ and ⟨111⟩ respect to the plane normal through a color-coded triangle. SS-BM (Fig. 9(a)) has equiaxed austenite grains with more random orientations instead of the preferred orientation of

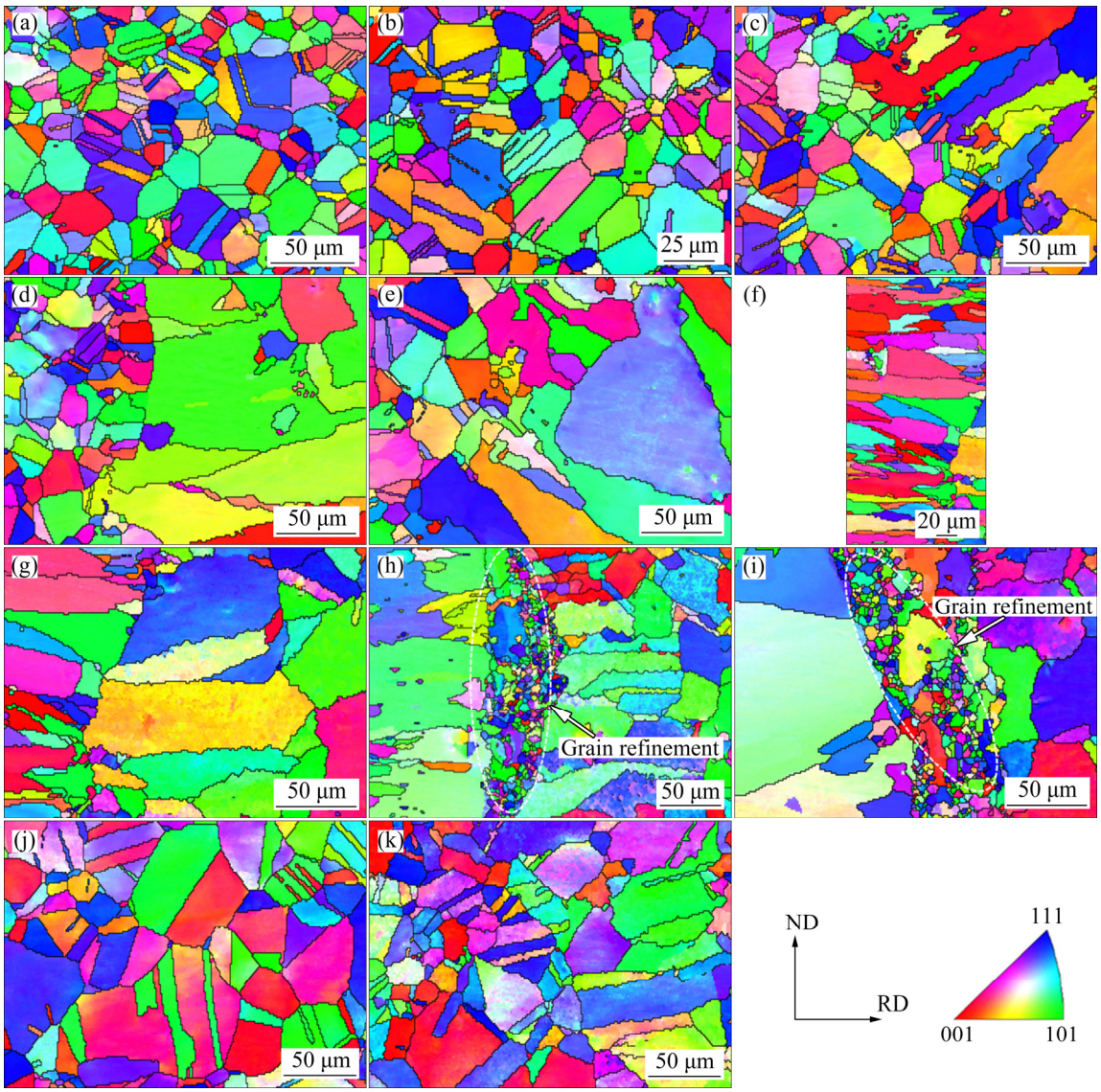

Fig. 9 EBSD-IPF micrographs of local weld sub-regions: (a) SS-BM; (b) SS-HAZ; (c) S1; (d) S2; (e) S3; (f) Fusion zone; (g) C1; (h) C2; (i) C3; (j) Cu-HAZ; (k) Cu-BM

the FCC. Figure 9(b) shows a very narrow SS-HAZ due to the high cooling rate of LBW process. It is noticed that the large-scale of grains in the SS-BM and SS-HAZ zones have their growth along the ND (normal direction), and only a few grains are grown along the RD (radial direction). All the IPF maps (Figs. 9(c−e)) received from the respective SS−weld interfaces (S1, S2 and S3) have course columnar grains spatially positioned on the fusion line with the clear epitaxial grain growth. The columnar grains had a consistent grain growth in line with the direction of weld heat flow, i.e., perpendicular to the fusion line. As a result of combined heterogeneous nucleation and constitutional supercooling effects, the weld fusion zone has elongated equiaxed grains (Fig. 9(f)).

It is notable that this feature was observed only in the SEM−EBSD micrographs and not able to achieve in the normal SEM micrographs. This is due to the differences in the spatial resolution between the SEM and SEM−EBSD techniques. The C1 interface (Fig. 9(g)) captured close to the fusion zone has coarse Cu grains with high aspect ratio located normal to the fusion line similar to the microstructural features noticed in S1. Both C2 and C3 interfaces (Fig. 9(h) and Fig. 9(i)) have a significant proportion of very fine grains produced from the outcome of thermal undercooling effects of LBW process and heterogeneous nucleation mechanism. The C2 and C3 interfaces also have columnar and equiaxed grain growths, respectively, in the region adjacent to the fine grain regions. It is expected that the grain refinement mechanism of these interfaces (C2 and C3) could lead to microhardness enhancement. In spite of minor heat input along the Cu side, the grain growth clearly appears in the Cu-HAZ (Fig. 9(j)) compared to the Cu-BM (Fig. 9(k)).

3.4.2 Grain misorientations

Figure 10 shows the grain boundary distributions of the weld sub-regions. All grains with a misorientation angle in the range of 2°−15° were accounted as low-angle boundaries (LABs), and the remaining grains (>15°) were considered as high-angle boundaries (HABs) [48]. In comparison to the SS-BM, the SS−weld interfaces (S1, S2 and S3) have more fractions of HABs than LABs. This is because, the laser heat received in the fusion zone was transferred through the SS−weld interface and resulted in a distinct boundary between the coarse grains without forming any sub-structured grains. Due to the laser beam offsets towards the SS, the misorientation profile of the fusion zone (LABs 27.1% and HABs 72.9%) is almost equivalent to that of the SS−weld interfaces. It is noted that the misorientation trends of the Cu−weld interfaces (C1, C2 and C3) are entirely inverse to those of the SS−weld interfaces (S1, S2 and S3) by occupying more proportion of LABs than HABs. The grain refinements produced along the Cu−weld interfaces by the constitutional supercooling effects have become responsible for the generation of LABs between the sub-structured grains. All the local misorientations information highlights the existing crystallographic relationships between the grain morphology and its corresponding grain misorientations.

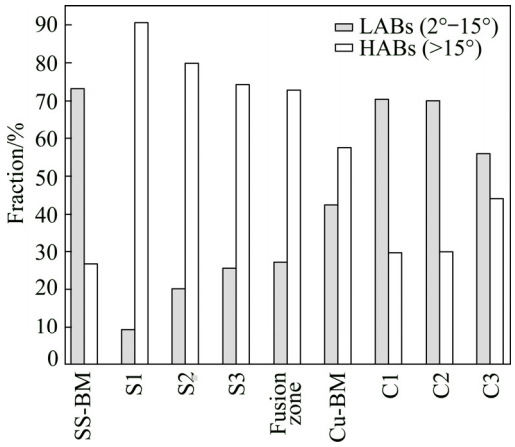

Fig. 10 Grain misorientation distributions of local weld zones

3.4.3 Grain size statistics

The grain size statistics are derived from the post-processed grain maps. The average grain size of SS-BM ((20.63±6.09) μm) and SS-HAZ ((21.20±5.81) μm) regions are very close to each other with minimum standard variations. It is noted that the average grain size is gradually increased towards the SS−weld interfaces, and their entire average grain size is equivalent to the average grain size of the fusion zone ((25.89±10.24) μm). Along the Cu side, the average grain size of Cu-BM ((24.81±9.90) μm) and Cu-HAZ ((25.47±9.72) μm) regions are almost the same. Among all weld sub-regions, C1 has the maximum average grain size of (30.92±15.77) μm. Average grain sizes of C2 ((22.60±17.31) μm) and C3 ((21.41±15.10) μm) interfaces are much smaller than its BM and fusion

zone due to the substantial occupation of fine grains in these interfaces. Because of various solidification effects and thermal gradients along the interfaces, both the weld interfaces (Cu and SS) have more standard deviations in their grain size compared to their respective BMs.

3.5 Tensile properties and impact toughness of welded joints

The average tensile properties derived from the uniaxial tensile tests are reported in Table 3. The UTS achieved by the joint is (236±3.75) MPa, which is found to be 84.28% that of the Cu-BM. In addition, other tensile properties such as elongation and fracture strain of the joint are determined as 5% and 0.20±0.01, respectively. These results are very close to the studies reported in Refs. [34,35]. The majority of fusion welding processes usually lead to abnormal grain growth through a range of solidification modes and result in the reduced tensile properties of the joint [46]. In the case of the dissimilar welding process, the reasons mentioned above are further exaggerated by the compositional gradients between two dissimilar materials. It is important to note that the tensile properties of the weld reported in this study are closely aligned with the weak base material of the dissimilar material system, i.e., Cu. Moreover, all the tensile specimens have fractured at the Cu−weld interface instead of fusion zone. This proves that the failure location of the dissimilar joint was entirely dominated by the weak and softened base material (Cu). The tensile fractographs received from the failure location (as shown in Figs. 11(a, b)) clearly show a sign of

Table 3 Tensile and impact test results of base metals and welded joints

Tensile specimen	Yield strength/MPa	Ultimate tensile strength/MPa	Fracture strain	Elongation/ %	Impact toughness/J
SS-BM	462±9	630±12	0.32±0.04	25±1	94±5
Cu-BM	142±6	280±8	0.46±0.05	31±2	65±7
Cu−SS joints	193±11.10	236±3.75	0.20±0.01	5±1	75±10
Cu−SS-HAZ	−	−	−	−	60±18

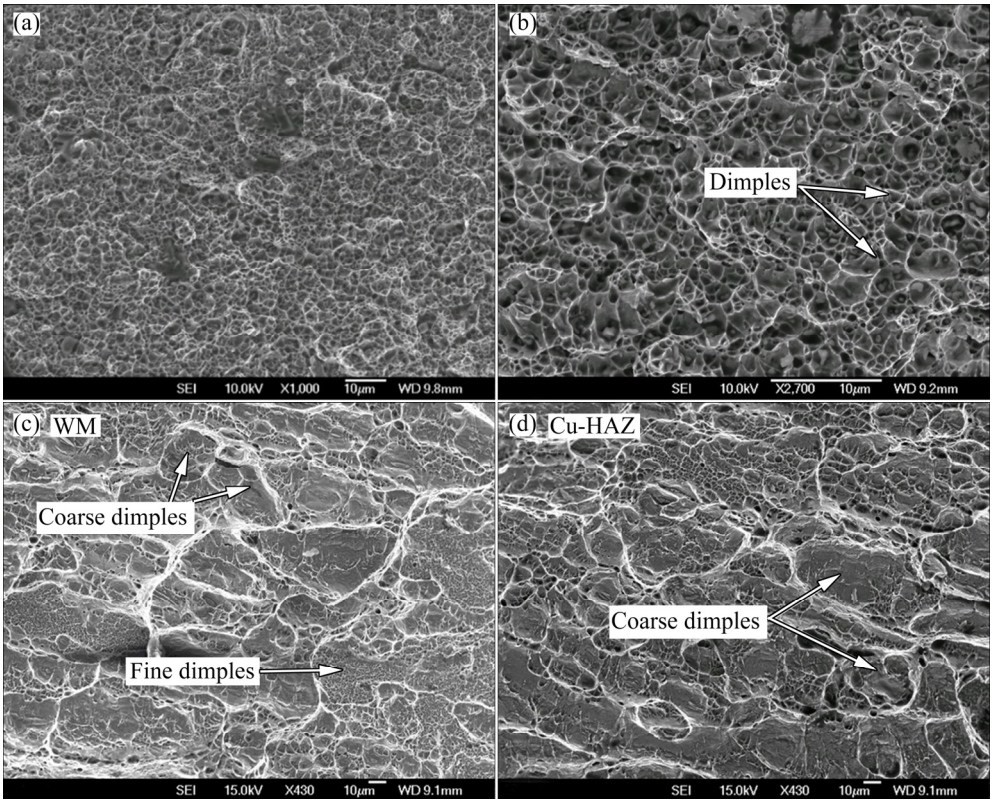

Fig. 11 SEM fractogrphs of tensile (a, b) and impact (c, d) specimens

plastic deformation based ductile failure in the form of dimples.

From the impact tests, it is determined that the weld joint has higher toughness than the weak base metal (i.e., Cu). Impact toughness specimens with the notch positioned at the weld center have absorbed 14.66% higher energy than the Cu-BM. However, the specimen that had the notch located at the Cu-HAZ has considerably lower impact properties compared to the center notch specimens. It is noticeable that all the standard impact toughness specimens have fractured in the region close to the Cu−weld interface, as observed in the tensile tests. The impact fractography of weld metal (WM) has both coarse and fine dimples (as shown in Fig. 11(c)). However, the impact fractography of Cu-HAZ shown in Fig. 11(d) has been majorly occupied with coarse dimples, which reduced the impact toughness of this zone. The results obtained from standard impact experiments followed by the fractography findings confirmed the high impact toughness property of the weld compared to the Cu-HAZ.

3.6 Microhardness measurements

Figure 12(a) shows the optical micrograph of the microhardness indents spatially positioned on the ROI as shown in Fig. 4. The microhardness variations in the primary locations of the weld, such as fusion zone and weld interfaces are correlated with their micrographs (as shown in Figs. 3(a, c)). Figure 12(b) shows the hardness contour plot derived from the microhardness measurements across the weld cross-section. Both base metals (SS (207±17) HV and Cu (91±8) HV) have more uniform hardness distributions equivalent to their theoretically expected hardness values. Additionally, the SS-BM and its HAZ have the same hardness due to the small heat input received from the laser, which significantly reduced the grain growth in the vicinity of the weld. However, excessive hardness gradients are revealed in the fusion zone. Even though the laser beam was completely offset towards the SS side, the large hardness fluctuations (143−263 HV) in the fusion zone was caused by the minor penetration of partially melted Cu metals.

The entry of Cu into the Fe-rich fusion zone,

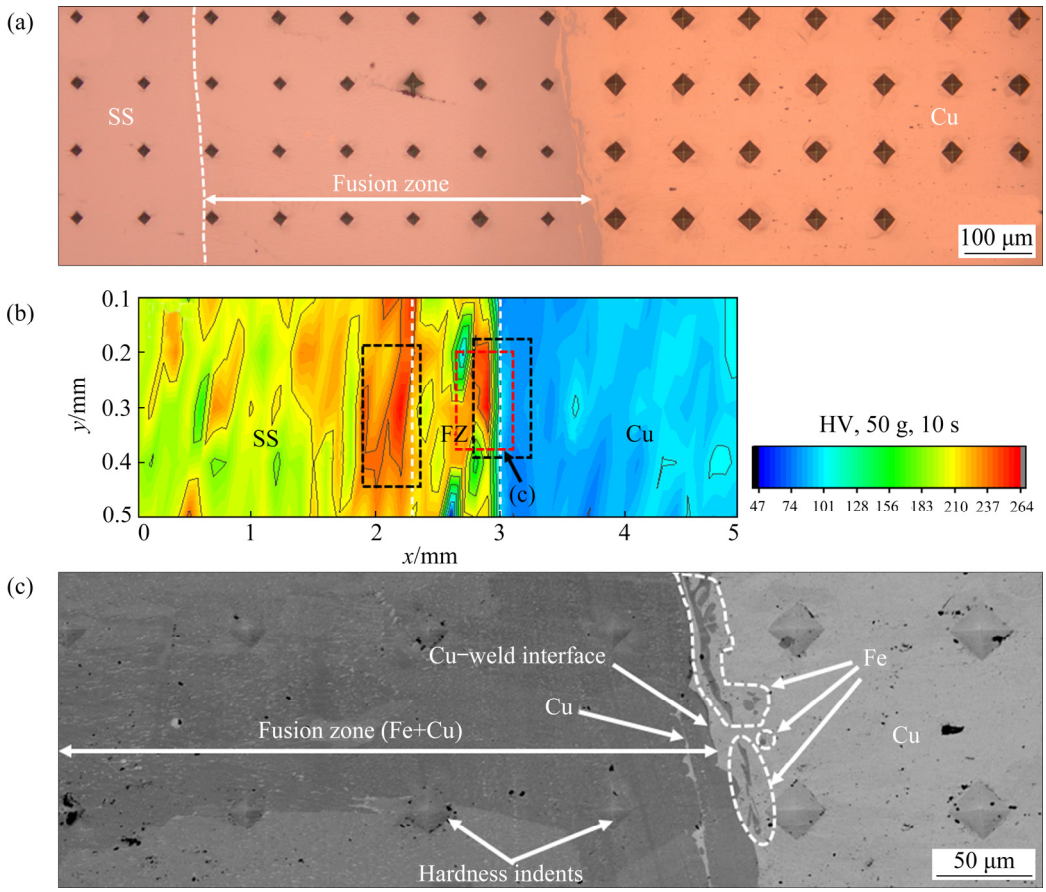

Fig. 12 Microhardness variations of local weld zones: (a) OM showing HV indents; (b) Microhardness contour plot; (c) SEM/BSE showing HV indents of Cu−weld interface

as evidenced in the backscattered SEM micrograph (Fig. 12(c)) could lead to local compositional variations in this zone. However, due to the minimal solubility of Cu in Fe, there is more possibility for the existence of unmixed spots in the dissimilar fusion weld zone. It is significant to note that tensile and impact specimens have failed in the region (Cu−weld interface) close to the unmixed spots. The combined compositional changes and unmixed spots have made the fusion zone hardness gradients compared to other weld zones. The average hardness value measured in the fusion zone is (216±22) HV. This hardness value is slightly above that of the SS-BM due to the presence of fine cellular grains along with the coarse columnar grains. PHANIKUMAR et al [32] also had this phenomenon in their investigation. Furthermore, a high standard deviation in the hardness measurements on the fusion zone indicates the scattering of Cu elements in the fusion zone. It is noteworthy that a sharp spike in the hardness is noted in the SS−weld interface ((241±12) HV). The fusion zone which had a major heat input from the laser heat source has attained the mixture of coarse columnar grains and fine cellular dendrites. The SS−weld interface adjacent to the fusion zone had a minimum heat input and high cooling rate in comparison to the fusion zone, and therefore these effects have produced the fine cellular dendritic microstructures throughout the SS−weld interface. The consistency in the formation of fine cellular dendrites at the SS−weld interface (as shown in Fig. 3(a)) has led to higher microhardness at this zone than the fusion zone of LBW (Cu−SS). SOLTANI and TAYEBI [43] supported the similar trends in their investigation.

As the laser beam was offset towards the SS, only a marginal amount of Cu melted into the fusion zone, and therefore no abnormal grain growth is found between the fusion zone and Cu−weld interface regions (Fig. 13(c)). Moreover, the high thermal conductivity of Cu has led to more heat dissipation away from the fusion zone and resulted in the unmixed zone with fine recrystallized grains as located in Fig. 3(c). Hence, the fine recrystallized grains with scattered Fe fragments have facilitated the hardness elevation at the Cu−weld interface. Although the LBW process always leads to a narrow HAZ, a slight drop in the hardness is visible at Cu-HAZ due to a minor grain growth gained from the laser heat convection (as shown in Fig. 3(c)). Thus, the hardness measured on the local weld zones is associated with their grain size evolved from the weld thermal cycle. It is more apparent that the microstructure with fine grain morphology has more resistance to the dislocation movements than the coarse grains due to the presence of large scale of grain boundaries. Hence, this crucial property of fine grain microstructure is responsible for the hardness enhancement. The findings from the microhardness along with the micrographs have corroborated the microstructure−mechanical property relationships of the weld.

4 Discussion on grain refinement mechanism of Cu−weld interface

From detailed microstructural characterizations performed on the various locations across the Cu−weld interface, it is evident that the Cu−weld interface had the rich microstructural gradients. The microstructural transformation along the Cu−weld interface is schematically illustrated in Fig. 13(a). It is noteworthy that the microstructure varies from the course columnar grains to equiaxed fine grains according to the thermal gradients received along the through-thickness direction of the Cu−weld interface. As the laser was offset towards the SS, the varying heat input transportation through the laser heat convection between SS and Cu−weld interface is the primary reason for the creation of completely melted and partially melted zones in the Cu−weld interface (as mapped in Fig. 13(a)). The fine equiaxed microstructure has been commonly observed across the weld manufactured by the FSW process due to the plastic deformation and friction heat generation mechanisms of this process. However, the grain refinement mechanism during the fusion welding process such as LBW process is primarily due to the heterogeneous nucleation assisted with the constitutional supercooling offered by the LBW process [47]. From this view, it is confident to claim that the heterogeneous nucleation was responsible for producing the equiaxed fine grains along the Cu−weld interface. However, the element that triggered the heterogeneous nucleation has not been confirmed in this study. It is interesting to note that the grain refinement mechanism was localized only at the C2

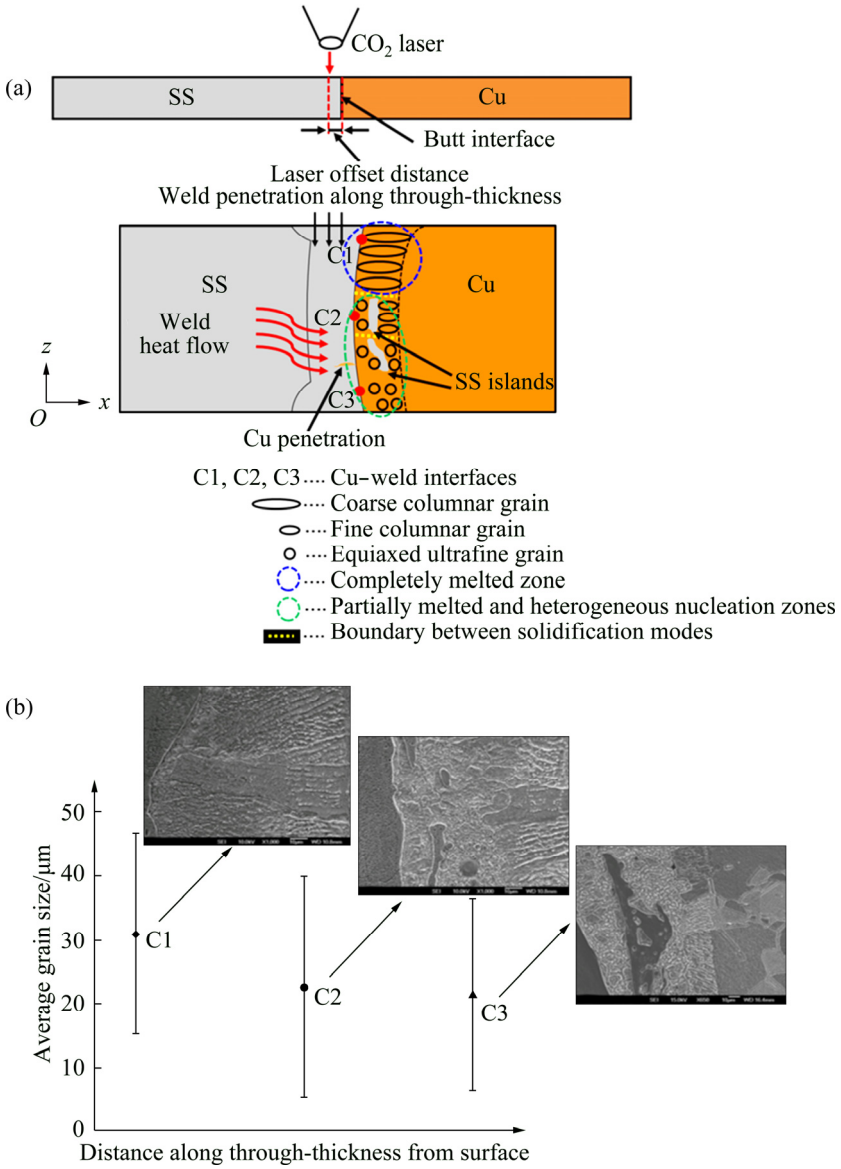

Fig. 13 Grain refinement mechanism of Cu−weld interface: (a) Schematic illustration of solidifications modes along Cu−weld interface; (b) Grain size evolution along through-thickness direction of Cu−weld interface

and C3 interfaces, and also the mechanism was more active in the C3 than C2. This made the C2 interface have a mixture of columnar and equiaxed fine grains instead of complete equiaxed fine grains as observed on the C3.

Furthermore, both C2 and C3 regions have the compositional gradients caused by the local penetration of SS elements into the Cu as well as some minor Cu elements channeled into the fusion zone. As per the Hall−Petch equation shown in Eq. (2), the mechanical performance especially the yield strength of any metal is proportional to its grain size:

$$\sigma_y = \sigma_0 + \frac{K}{\sqrt{d}} \quad (2)$$

where σ_y is the yield strength, σ_0 is the materials constant, K is the strengthening coefficient, and d is the grain size. Therefore, the varying grain size along the Cu−weld interface, as shown in Fig. 13(b) will lead to yield strength variations during the post-elastic deformation of the joint.

Even though this variation was qualitatively observed in terms of microhardness measurements of this investigation, there is a definite necessity to involve a full-field technique such as digital image correlation (DIC) to assess the local strain distributions on the Cu−weld interface. On the other hand, it is much believed that the fine grains have higher strength as well as higher resistance to the solidification cracking compared to the coarse

grains. Therefore, the strength and reliability of an LBW (Cu−SS) weld could be enhanced by achieving a high density of fine grains as observed on the C2 and C3 interfaces. This could be accomplished by externally stimulating the heterogeneous nucleation spots during the welding process, which will further increase the quantity of fine equiaxed grains along the Cu−weld interface.

5 Conclusions

(1) The primary process parameters of LBW that have a significant impact on the quality of the (Cu−SS) joint were determined as laser power, welding speed, and laser beam offset conditions. Optical micrographs identified that both the SS−weld interface and fusion zone had a cellular dendritic microstructure. Along the Cu side, the Cu−weld interface had equal proportions of coarse columnar and fine Cu grains.

(2) SEM/BSE and SEM/EDS micrographs obtained from the weld interfaces and fusion zone have demonstrated the highly heterogeneous microstructures interlinked with phase and composition details.

(3) EBSD micrographs of SS−weld interfaces and fusion zone have evidenced that all these regions had a distinct grain morphology. The grain refinement zone was spotted in the Cu−weld interface.

(4) The LBW (Cu−SS) joints have achieved 85% tensile strength (UTS of (236±4) MPa) of the weak base metal (Cu). All the tensile specimens have failed at the Cu−weld interface, and the nature of the tensile failure was identified to be ductile.

(5) Microhardness measurements revealed that the SS−weld interface ((241±12) HV) had the highest hardness among all local weld zones. The fusion zone had large hardness gradients due to the presence of Cu and SS elements with the average hardness value of (216±22) HV.

References

[1] SAFARBALI B, SHAMANIAN M, ESLAMI A. Effect of post-weld heat treatment on joint properties of dissimilar friction stir welded 2024-T4 and 7075-T6 aluminum alloys [J]. Transactions of Nonferrous Metals Society of China, 2018, 28: 1287−1297.

[2] DONATUS U, THOMPSON G E, MOMOH M I, MALEDI N B, TSAI I L, FERREIRA R O, LIU Z. Variations in stir zone and thermomechanically affected zone of dissimilar friction stir weld of AA5083 and AA6082 alloys [J]. Transactions of Nonferrous Metals Society of China, 2018, 28: 2410−2418.

[3] KHOJASTEHNEZHAD M V, POURASL H H. Microstructural characterization and mechanical properties of aluminum 6061-T6 plates welded with copper insert plate (Al/Cu/Al) using friction stir welding [J]. Transactions of Nonferrous Metals Society of China, 2018, 28: 415−426.

[4] XUE Jun-yu, LI Yuan-xing, CHEN Hui, ZHU Zong-tao. Wettability, microstructure and properties of 6061 aluminum alloy/304 stainless steel butt joint achieved by laser-metal inert-gas hybrid welding-brazing [J]. Transactions of Nonferrous Metals Society of China, 2018, 28: 1938−1946.

[5] MARTINSEN K, HU S J, CARLSON B E. Joining of dissimilar materials [J]. CIRP Annals−Manufacturing Technology, 2015, 64: 679−699.

[6] DENG Yun-hua, GUAN Qiao, TAO Jun. Effect of heating time on bonding interface, atom diffusion and mechanical properties of dissimilar titanium joints produced by thermal self-compressing bonding [J]. Transactions of Nonferrous Metals Society of China, 2018, 28: 662−668.

[7] XU Wei-feng, ZHANG Zhen-lin. Microstructure and mechanical properties of laser beam welded TC4/TA15 dissimilar joints [J]. Transactions of Nonferrous Metals Society of China, 2016, 26: 3135−3146.

[8] YANG Jin, LI Yu-long, ZHANG Hua. Microstructure and mechanical properties of pulsed laser welded Al/steel dissimilar joint [J]. Transactions of Nonferrous Metals Society of China, 2016, 26: 994−1002.

[9] QIN Guo-liang, SU Yu-hu, WANG Shu-jun. Microstructures and properties of welded joint of aluminum alloy to galvanized steel by Nd:YAG laser + MIG arc hybrid brazing-fusion welding [J]. Transactions of Nonferrous Metals Society of China, 2014, 24: 989−995.

[10] MASOUDIAN A, TAHAEI A, SHAKIBA A, SHARIFIANJAZI F, MOHANDESI J A. Microstructure and mechanical properties of friction stir weld of dissimilar AZ31-O magnesium alloy to 6061-T6 aluminum alloy [J]. Transactions of Nonferrous Metals Society of China, 2014, 24: 1317−1322.

[11] KUMAR N, MISHRA R S. Friction stir welding of dissimilar alloys and materials [M]. UK: Butterworth-Heinemann, 2015.

[12] LIPA M, DUROCHER A, TIVEY R, HUBER T, SCHEDLER B, WEIGERT J. The use of copper alloy CuCrZr as a structural material for actively cooled plasma facing and in vessel components [J]. Fusion Engineering and Design, 2005, 75−79: 469−473.

[13] DAVIS J W, KALININ G M. Material properties and design requirements for copper alloys used in ITER [J]. Journal of Nuclear Materials, 1998, 258−263: 323−328.

[14] WANG Yu-xin, LI Xiao-jie, WANG Xiao-hong, YAN Hong-hao. Fabrication of a thick copper-stainless steel clad plate for nuclear fusion equipment by explosive welding [J]. Fusion Engineering and Design, 2018, 137: 91−96.

[15] RAMIREZ A J, BENATI D M. Effect of tool offset on dissimilar Cu-AISI 316 stainless steel friction stir welding [C]//Proc Twenty-first International Offshore and Polar

Engineering Conference 2011. Hawaii: ISOPE, 2011: 548−552.

[16] LUSCH C, BORSCH M, HEIDT C, MAGGINETTI N, SAS J, WEISS K P, GROHMANN S. Qualification of electron-beam welded joints between copper and stainless steel for cryogenic application [C]//Proc Materials Science and Engineering. USA: IOP, 2015: 012017.

[17] JOSHI R G, BADHEKA V. Microstructures and properties of copper to stainless steel joints by hybrid FSW [J]. Metallography, Microstructure, and Analysis, 2017, 6: 470−480.

[18] JAFARI M, ABBASI M, POURSINA D, GHEYSARIAN A, BAGHERI B. Microstructures and mechanical properties of friction stir welded dissimilar steel−copper joints [J]. Journal of Mechanical Science and Technology, 2017, 31: 1135−1142.

[19] IMANI Y, BESHARATI M K, GUILLOT M. Improving friction stir welding between copper and 304L stainless steel [J]. Advanced Materials Research, 2011, 409: 263−268.

[20] SAHLOT P, NENE S S, FRANK M, MISHRA R S, ARORA A. Towards attaining dissimilar lap joint of CuCrZr alloy and 316L stainless steel using friction stir welding [J]. Science and Technology of Welding and Joining, 2018, 23: 715−720.

[21] SHOKRI V, SADEGHI A, SADEGHI M H. Effect of friction stir welding parameters on microstructure and mechanical properties of DSS−Cu joints [J]. Materials Science and Engineering A, 2017, 693: 111−120.

[22] WANG T, SHUKLA S, NENE S S, FRANK M, WHEELER W R, MISHRA R S. Towards obtaining sound butt joint between metallurgically immiscible pure Cu and stainless steel through friction stir welding [J]. Metallurgical and Materials Transactions A, 2018, 49: 2578−2582.

[23] SRINIVAS K, SARANARAYANAN R, LAKSHMINARAYANAN A K, SRINIVASAN N, VENKATRAMAN B. Zone wise properties of friction stir welded copper–stainless steel joints using digital image correlation [J]. Applied Mechanics and Materials, 2015, 787: 485−489.

[24] ZHANG Heng, JIAO Ke-xin, ZHANG Jian-liang, LIU Jian-ping. Microstructure and mechanical properties investigations of copper−steel composite fabricated by explosive welding [J]. Materials Science and Engineering A, 2018, 731: 278−287.

[25] DURGUTLU A, GÜLENÇ B, FINDIK F. Examination of copper/stainless steel joints formed by explosive welding [J]. Materials and Design, 2005, 26: 497−507.

[26] KAR J, ROY S K, ROY G G. Effect of beam oscillation on electron beam welding of copper with AISI-304 stainless steel [J]. Journal of Materials Processing Technology, 2016, 233: 174−185.

[27] MAGNABOSCO I, FERRO P, BONOLLO F, ARNBERG L. An investigation of fusion zone microstructures in electron beam welding of copper–stainless steel [J]. Materials Science and Engineering A, 2006, 424: 163−173.

[28] SHIRI S G, NAZARZADEH M, SHARIFITABAR M, AFARANI M S. Gas tungsten arc welding of CP-copper to 304 stainless steel using different filler materials [J]. Transactions of Nonferrous Metals Society of China, 2012, 22: 2937−2942.

[29] CHANG Chin-chun, WU Ling-hui, SHUEH Chin, CHAN Che-kai, SHEN I-ching, KUAN Chien-kuang. Evaluation of microstructure and mechanical properties of dissimilar welding of copper alloy and stainless steel [J]. The International Journal of Advanced Manufacturing Technology, 2017, 91: 2217−2224.

[30] CHENG Zhi, HUANG Ji-hua, YE Zheng, CHEN Yu, YANG Jian, CHEN Shu-hai. Microstructures and mechanical properties of copper−stainless steel butt-welded joints by MIG-TIG double-sided arc welding [J]. Journal of Materials Processing Technology, 2019, 265: 87−98.

[31] SARANARAYANAN R, LAKSHMINARAYANAN A K, VENKATRAMAN B. A combined full-field imaging and metallography approach to assess the local properties of gas tungsten arc welded copper–stainless steel joints [J]. Archives of Civil and Mechanical Engineering, 2019, 19: 251−267.

[32] PHANIKUMAR G, MANJINI S, DUTTA P, CHATTOPADHYAY K, MAZUMDER J. Characterization of a continuous CO_2 laser-welded Fe−Cu dissimilar couple [J]. Metallurgical and Materials Transactions A, 2005, 36: 2137−2147.

[33] MENG Yun-fei, LI Xin-wei, GAO Ming, ZENG Xiao-yan. Microstructures and mechanical properties of laser-arc hybrid welded dissimilar pure copper to stainless steel [J]. Optics and Laser Technology, 2019, 111: 140−145.

[34] SORENSEN D, PISCHLAR J, STEVICK J, HINTSALA E, STAUFFER D, MYERS J C, KEENAN T, RAMIREZ A J. Investigation of a dissimilar vitreloy 105 to grade 2 titanium laser weld [J]. Materials Science and Engineering A, 2019, 742: 33−43.

[35] MAI T A, SPOWAGE A C. Characterisation of dissimilar joints in laser welding of steel–kovar, copper–steel and copper–aluminium [J]. Materials Science and Engineering A, 2004, 374: 224−233.

[36] YAO Cheng-wu, XU Bin-shi, ZHANG Xian-cheng, HUANG Jian, FU Jan, WU Yi-xiong. Interface microstructure and mechanical properties of laser welding copper–steel dissimilar joint [J]. Optics and Lasers in Engineering, 2009, 47: 807−814.

[37] CHEN Shu-hai, HUANG Ji-hua, XIA Jun, ZHAO Xing-ke, LIN San-bao. Influence of processing parameters on the characteristics of stainless steel/copper laser welding [J]. Journal of Materials Processing Technology, 2015, 222: 43−51.

[38] CHEN Shu-hai, HUANG Ji-hua, XIA Jun, ZHAO Xing-ke. Microstructural characteristics of a stainless steel/copper dissimilar joint made by laser welding [J]. Metallurgical and Materials Transactions A, 2013, 44: 3690−3696.

[39] MANNUCCI A, TOMASHCHUK I, VIGNAL V, SALLAMAND P, DUBAND M. Parametric study of laser welding of copper to austenitic stainless steel [J]. Procedia CIRP, 2018, 74: 450−455.

[40] ASTM E8/E8M-16a. Test methods for tension testing of metallic materials [S]. West Conshohocken, PA: ASTM International, 2016.

[41] ASTM E23-12c. Test methods for notched bar impact testing of metallic materials [S]. West Conshohocken, PA: ASTM International, 2012.

[42] ASTM E384-17. Test method for microindentation hardness of materials [S]. West Conshohocken, PA: ASTM International, 2017.
[43] SOLTANI H M, TAYEBI M. Comparative study of AISI 304L to AISI 316L stainless steels joints by TIG and Nd:YAG laser welding [J]. Journal of Alloys and Compounds, 2018, 767: 112−121.
[44] GAO Z, JIANG P, MI G, CAO L, LIU W. Investigation on the weld bead profile transformation with the keyhole and molten pool dynamic behavior simulation in high power laser welding [J]. International Journal of Heat and Mass Transfer, 2018, 116: 1304−1313.
[45] GOLDSTEIN J I, NEWBURY D E, MICHAEL J R, RITCHIE N W M, SCOTT J H J, JOY D C. Scanning electron microscopy and X-ray microanalysis [M]. 4th ed. New York: Springer, 2018.
[46] KOU S. Welding metallurgy [M]. 2nd ed. United States: John Wiley & Sons Inc, 2003.
[47] LIPPOLD J C, DUPONT J N. Welding metallurgy and weldability of nickel-base alloys [M]. United States: John Wiley & Sons Inc, 2009.
[48] MAITLAND T, SITZMAN S. Backscattering detector and ebsd in nanomaterials characterization. scanning microscopy for nanotechnology: Techniques and applications [M]. New York: Springer, 2007.

激光焊接铜与不锈钢接头之间焊缝区显微组织的非均匀性

Saranarayanan RAMACHANDRAN, A. K. LAKSHMINARAYANAN

Department of Mechanical Engineering, SSN College of Engineering, Kalavakkam 603103, Tamil Nadu, India

摘　要：研究激光焊接 (LBW)工艺对铜(Cu)和不锈钢(SS)异种焊缝显微组织与力学性能关系的影响。采用背散射(BSE)扫描电子显微镜(SEM)成像来表征 LBW (Cu−SS)焊缝的高度非均匀组织特征。BSE 分析充分证明在异种焊接界面和熔合区产生复杂的显微组织。沿铜/焊缝界面存在明显的晶粒生长差异：从粗柱状晶到等轴状超细晶。高分辨电子背散射衍射(EBSD)分析证实铜/焊缝界面存在晶粒细化机制。拉伸和冲击试验结果表明，异种焊缝的拉伸和冲击性能与铜基体的基本一致。在熔合区和铜/焊接界面区等非均匀材料成分区，存在明显的显微硬度梯度。为了全面了解局部焊缝亚区的组织与性能的关系，确定出焊缝亚区的异质形核点，并与显微硬度测试结果相互关联。

关键词：激光焊接；铜；不锈钢；显微组织表征；拉伸性能；冲击韧性

(Edited by Bing YANG)